ADVANCED MATERIALS
www.advmat.de

Rafting-Enabled Recovery Avoids Recrystallization in 3D-Printing-Repaired Single-Crystal Superalloys

Kai Chen, Runqiu Huang, Yao Li, Sicong Lin, Wenxin Zhu, Nobumichi Tamura, Ju Li,* Zhi-Wei Shan,* and Evan Ma**

The repair of damaged Ni-based superalloy single-crystal turbine blades has been a long-standing challenge. Additive manufacturing by an electron beam is promising to this end, but there is a formidable obstacle: either the residual stress and γ/γ' microstructure in the single-crystalline fusion zone after e-beam melting are unacceptable (e.g., prone to cracking), or, after solutionizing heat treatment, recrystallization occurs, bringing forth new grains that degrade the high-temperature creep properties. Here, a post-3D printing recovery protocol is designed that eliminates the driving force for recrystallization, namely, the stored energy associated with the high retained dislocation density, prior to standard solution treatment and aging. The post-electron-beam-melting, pre-solutionizing recovery via sub-solvus annealing is rendered possible by the rafting (i.e., directional coarsening) of γ' particles that facilitates dislocation rearrangement and annihilation. The rafted microstructure is removed in subsequent solution treatment, leaving behind a damage-free and residual-stress-free single crystal with uniform γ' precipitates indistinguishable from the rest of the turbine blade. This discovery offers a practical means to keep 3D-printed single crystals from cracking due to unrelieved residual stress, or stress-relieved but recrystallizing into a polycrystalline microstructure, paving the way for additive manufacturing to repair, restore, and reshape any superalloy single-crystal product.

Modern turbine blades are made of superalloy single crystals, strengthened by cuboidal precipitates of ordered γ'-phase in the γ-phase matrix.[1] Single-crystal Ni-based superalloys outperform their polycrystalline counterparts by a large margin, in many aspects including the resistance to creep, fatigue, and oxidation,[2] by eliminating most of the defects that form during casting. These high-value single-crystal blades are nonetheless subjected to surface damage and cracking upon extensive service in harsh environments. It is thus critical to find a way to repair the damaged surface while keeping their single-crystalline nature as well as the desired uniform γ/γ' microstructure. Such a successful repair will extend the life of turbine blades and reduce the overall cost significantly.

The versatile 3D-printing technique emerging in recent years appears to be a powerful route toward this goal.[3] Via "epitaxial" deposition of the alloy, one layer at a time, additive manufacturing can preserve the crystallographic orientation of the substrate single crystal.[4–11] However, as 3D printing involves fast cooling, the γ' precipitates are either undetectable[12] or excessively small with uneven sizes and rounded corners[13,14] and hence less stable during high-temperature service. At some superalloy compositions and 3D-printing parameters, detrimental Laves phase particles are reported.[15] More importantly, a high density of dislocations build up in the heat-affected zone (HAZ), due to unavoidable (often local) deformation under high thermal stresses during printing.[16,17] Upon solution treatment at elevated temperatures, these regions riddled with dislocations readily undergo recrystallization (RX)[18] that renders the microstructure polycrystalline, which would significantly degrade the high-temperature creep performance of blades (Figure S1 in

Prof. K. Chen, R. Huang, S. Lin, W. Zhu, Prof. Z.-W. Shan
Center for Advancing Materials Performance from the Nanoscale
State Key Laboratory for Mechanical Behavior of Materials
Xi'an Jiaotong University
Xi'an, Shaanxi 710049, P. R. China
E-mail: kc_xjtu@xjtu.edu.cn; zwshan@xjtu.edu.cn
Dr. Y. Li
School of Materials Science and Engineering
Chang'an University
Xi'an, Shaanxi 710064, P. R. China

The ORCID identification number(s) for the author(s) of this article can be found under https://doi.org/10.1002/adma.201907164.

DOI: 10.1002/adma.201907164

Dr. N. Tamura
Advanced Light Source
Lawrence Berkeley National Laboratory
Berkeley, CA 94720, USA
Prof. J. Li
Departments of Nuclear Science and Engineering
and Materials Science and Engineering
Massachusetts Institute of Technology
Cambridge, MA 02139, USA
E-mail: liju@mit.edu
Prof. E. Ma
Department of Materials Science and Engineering
Johns Hopkins University
Baltimore, MD 21218, USA
E-mail: ema@jhu.edu

the Supporting Information).[2] These shortcomings are in fact characteristic of all 3D-printed superalloys,[19] such that the repaired part is no longer as highly performing as the original single crystal. There is thus a pressing need to conceive an innovative treatment.

To this end, our strategy is to design post-3D-printing annealing to reduce the driving force for recrystallization that ruins the single-crystal structure. That is, we aim to remove the accumulated dislocations through a recovery heat treatment (HT) before the standard solution HT and aging HT. However, conventional wisdom is that recovery is difficult to realize in Ni-based superalloys for mainly two reasons. First, the stacking fault energy of Ni-based superalloys (<≈20 mJ m^{-2})[20,21] is much lower than that of pure Ni (125 mJ m^{-2})[22] and Al (166 mJ m^{-2}).[23] A low stacking fault energy promotes the unit dislocations to dissociate into partial dislocations, hampering their climb and cross slip, the basic mechanisms for recovery.[23,24] Second, the closely spaced γ' particles impede the motion of stored dislocations and hence prevent their annihilation at temperatures below the γ' solvus.[23,25,26] If, instead, the alloy is heated to temperatures above the γ' solvus, RX sets in quickly well before the stored dislocations are effectively removed via recovery.[24–27] Such an RX scenario is demonstrated in **Figure 1** (standard solution HT).

Herein, we demonstrate a novel HT to produce a repaired single crystal with γ/γ' microstructure indistinguishable from the interior. Prior to standard solution treatment where all the γ' disappear, dislocations (with associated excess energy) accumulated in the HAZ can already be annealed away by rafting-facilitated recovery, through annealing at an appropriate sub-solvus temperature. During such recovery annealing prior to solution HT, the cuboidal γ' precipitates become unstable and link together to form flat rafted precipitates in the HAZ. This greatly reduces the dislocation density, such that in subsequent solution and aging HT, using standard protocol normally used, RX does not get triggered to nucleate new grains.

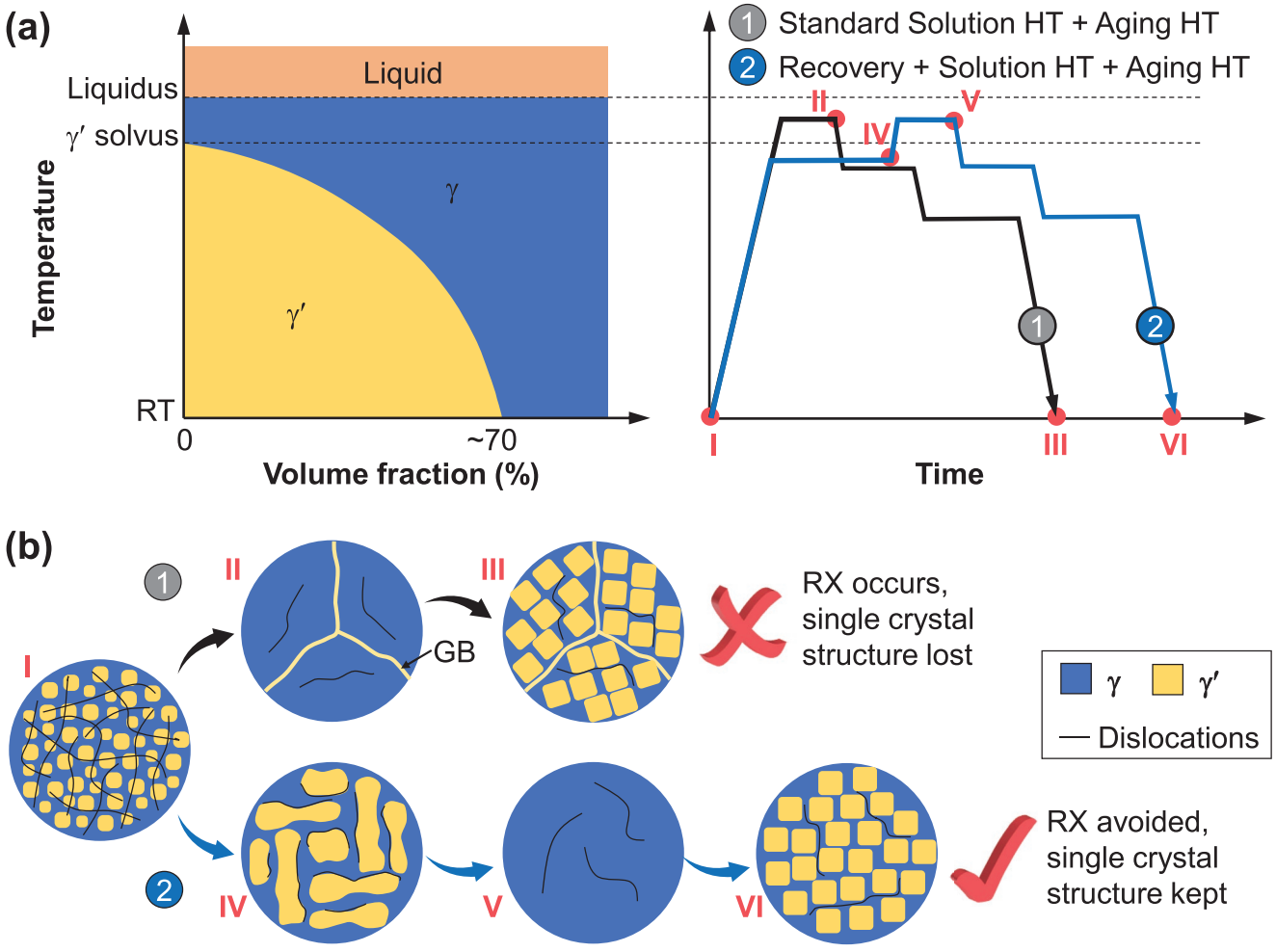

Figure 1. Microstructural evolution of 3D-printed Ni-based single crystals induced by standard solution HT, in comparison with our novel HT incorporating recovery annealing. a) Standard solution HT involves one-step annealing, while our new HT protocol includes a recovery annealing procedure prior to solution treatment. The aging HT is the same for both protocols. b) High density of dislocations are built in the as-printed sample, especially in HAZ (State I). RX triggered by the standard solution HT leads to the formation of high-angle grain boundaries (State II), and thus the single-crystalline nature is lost and the repairing practice is unsuccessful although the γ' particles are uniform after aging HT (State III). With the new HT, recovery annealing prior to the solution HT results in rafted structure (State IV) and assists the preemption of the RX during solution HT (State V). After aging HT, the γ' microstructure is uniform and the single-crystalline structure is kept (State VI).

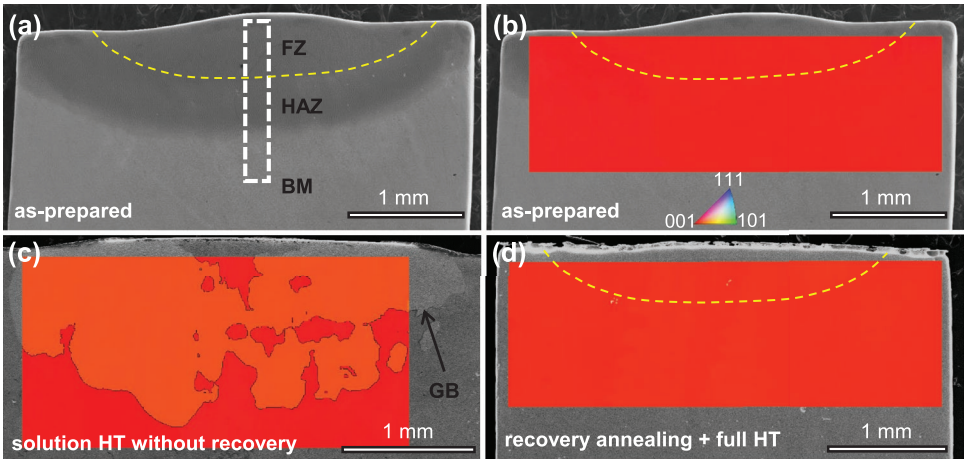

Figure 2. EBM samples before and after different HT protocols. a) Three regions are visible in the cross-sectional SEM image of the as-prepared sample: FZ, HAZ, and unaffected BM. b–d) EBSD orientation maps indicate that: b) the as-prepared EBM sample is a single crystal, but c) RX occurs and high-angle grain boundaries are generated upon solution HT at 1300 °C for 0.5 h, while d) the RX is successfully prevented to keep the single-crystalline nature by applying a recovery HT at 1100 °C for 6 h before standard HT.

Electron-beam melting (EBM) with no feedstock was carried out as an analog to 3D-printing repairing on AM3, a first-generation single-crystal Ni-based superalloy used as a model in this study. The electron beam was focused and programmed for line scans on the substrate (base metal, BM) surface of [001] cast single-crystal boule to generate fusion zones (FZs). **Figure 2** shows the morphology of the EBM sample and the crystal orientation distribution before and after HT using different protocols. In the low-magnification image, Figure 2a, three regions can be readily distinguished: un-affected BM, HAZ, and FZ. The crystal orientation is the same throughout the as-prepared EBM sample, from the BM to the HAZ to the FZ (Figure 2b). Detailed analysis proves the existence of slight lattice-orientation fluctuations caused by stored dislocations (Figure S2 in the Supporting Information). After solution HT at 1300 °C for 30 min without prior recovery annealing, RX grains and high-angle grain boundaries are clearly observed in both HAZ and FZ (Figure 2c). After RX, the residual strain is low, and the crystal orientation in each grain is uniform, indicating low dislocation density (Figures S3 and S4, Supporting Information). In contrast, after our new 1100 °C recovery annealing for 6 h prior to standard HT, the electron backscatter diffraction (EBSD) map shows no detectable RX grains (Figure 2d, and more detailed and complementary analysis in Figure S5, Supporting Information). In other words, the newly developed HT protocol fulfills the "keeping the single crystal" requirement. The other requirement that needs to be accomplished simultaneously is the "uniform γ' microstructure."

The EBM sample (Figure 2b) without HT does not fit the bill in this regard. There the fast cooling rate inherent to EBM produces not only much finer dendrites in the FZ compared to the cast counterpart, but also much smaller γ' precipitates—the average size is <50 nm (**Figure 3**a), only a quarter of that in the BM. A microstructure gradient is observed in the HAZ (in between the FZ and the BM). The upper HAZ near the fusion line has experienced a temperature sufficiently high to dissolve all the primary γ'. Thus, the small particles in the upper HAZ are re-precipitated γ', quite similar to those in the FZ. Moving down away from the fusion line, the peak temperature is lower and the period of time that the local temperature is above the γ' solvus is shorter, such that the primary γ' only dissolves partially. The subsequent re-precipitation at lowered temperatures forms fine secondary γ'. Together they constitute a bimodal γ' size distribution. The population of the secondary γ' decreases gradually with increasing distance, becoming completely undetectable in the region about 300 µm away from the fusion line, leaving only cuboidal primary γ' with side length in the 200–300 nm range. This kind of vertical variation in the γ/γ' microstructure is unacceptable, especially if one would like to scale this process by adding new powders to build up the part. Furthermore, as shown below, large residual stresses on the order of 0.6 GPa exist in the fast-cooled HAZ. Considering this HAZ is only ≈1 mm in thickness and one needs to build many similar zones on top of one another in the future, if unrelieved, such a large residual stress does not bode well for the buildability of larger parts, or for the fatigue life of the repaired part, since surface cracking is prone to occur near residual stresses.

After EBM, the crystal is riddled with dislocations and the elastic strain associated with them is distributed in an inhomogeneous manner. To see the latter, we have taken synchrotron X-ray microdiffraction (µXRD) across the FZ and the HAZ, covering an area of 80 µm (horizontal) × 1150 µm (vertical), as indicated using the boxed rectangle in Figure 2a, at 2 µm spatial resolution. From the orientation inverse pole figure maps (Figure S6 in the Supporting Information), it appears that the entire scanned area remains a single crystal and the dendrite growth is along the [001] direction. The vertical and horizontal components of the elastic strain tensor, denoted as ε_v and ε_h, respectively, are displayed in Figure 3b. In all regions from the BM through the HAZ to the FZ, these strains are found to vary considerably in magnitude from location to location, and even change sign. The BM substrate is under tension in the vertical direction but is compressed in the horizontal direction; this is related to the preprinting thermal history of the superalloy. The opposite is observed for strains in the HAZ: ε_h is tensile while ε_v is compressive. The transition from the BM to the

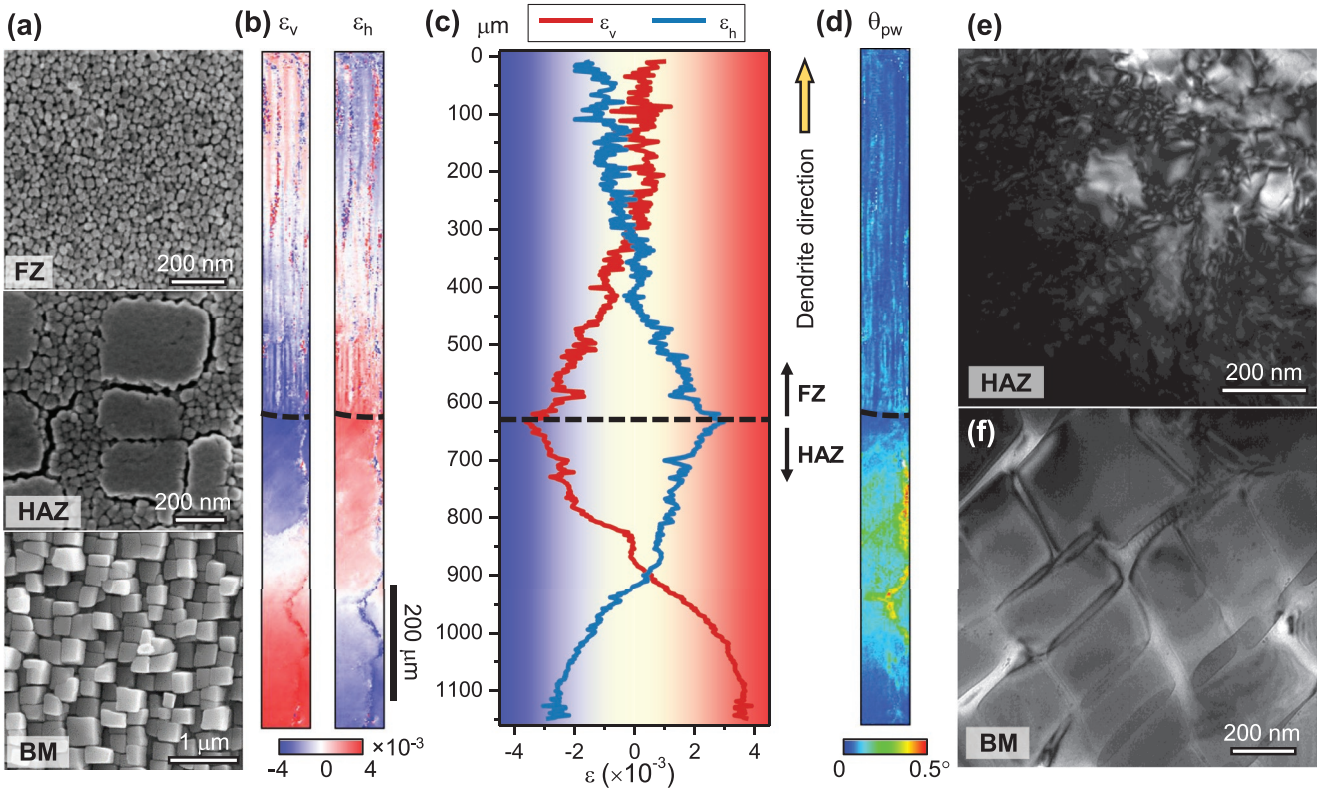

Figure 3. Inhomogeneous distributions of γ' morphology, elastic strain, and dislocations in the EBM sample. a) Distinctly different γ' morphologies in the FZ, HAZ, and BM, as displayed in their corresponding SEM images. b) 2D and c) 1D lattice elastic strain as well as d) diffraction peak width maps indicate nonuniform deformation. The fusion line is marked using a dashed line in (b)–(d). e,f) TEM images indicate that dislocations of high density are present in the HAZ (e), while the BM is almost dislocation free (f).

HAZ is smooth and gradual. Both ε_h and ε_v change sign about 300 μm away from the BM/HAZ interface. ε_h and ε_v reach their peak magnitudes at the HAZ/FZ interface, and then decrease together upon entering the FZ. The magnitude of the strain is highly variable in the FZ, and changes sign from the interdendritic regions to dendrite cores, due to nonuniform chemical and microstructure distribution. Considering the modulus of superalloy is of the order 200 GPa, we are facing peak tensile residual stress on the order of 0.6 GPa, which is unacceptable from scaling-up and surface cracking point of view. A high density of dislocations in the HAZ is reflected by the obviously broadened Laue peak width, see the colored peak width map in Figure 3d (although the dislocation density is difficult to quantify accurately from the peak width). In the FZ, the peak width map also exhibits fine stripe features, presumably attributable to the chemical and microstructural heterogeneities between dendrite cores and interdendritic regions. This evidence of a large population of dislocations in many local regions is consistent with the observation in the transmission electron microscopy (TEM) image of Figure 3e, in which the dislocation density is measured to be about 8×10^{14} m^{-2} using the line-intercept method introduced by Norfleet et al.[28] This value is for a small local region, but from the colored peak width map the dislocation density is inhomogeneous and should be higher in many other regions of the HAZ. Similar to previous reports for cast materials,[29] the BM is almost dislocation free (Figure 3f).

To relieve the residual stress (Figure 3b,c) and remove the γ/γ' microstructural variation (Figure 3a) in the single crystal, HT is necessary. But while the traditional above-solvus solutionizing HT (path 1 in Figure 1a) can relieve the residual stress and restore the desirable γ/γ' microstructure, this unfortunately leads to recrystallization (Figure 2c) which defeats the whole point of trying to 3D-print single-crystalline part. The dislocations and elastic energy stored are the root cause that drives RX upon the ensuing solutionizing treatment. Shortening of the solution treatment time reduced the area fraction of the RX grains, but was not able to avoid RX, unless the solution treatment is conducted at a temperature well below that needed to reach complete solid solution. At such a temperature, however, the solution treatment is ineffective to remove the chemical and microstructural heterogeneities from dendrites because it would not be able to solutionize the interdendritic region, where the elements promoting γ' formation are known to be enriched and thus the γ' solvus temperature is higher than that in the dendrite cores.

After incorporating our recovery annealing before solution HT (path 2 in Figure 1a), the microstructure becomes completely different from not only the reference sample (full HT after EBM without recovery annealing; as seen in Figure 2c, there RX is obvious, although the precipitates inside the grains have become uniform in size), but also the EBM sample (nonuniform microstructure, as discussed above with Figure 3). The γ' precipitates in the FZ, HAZ, and BM are

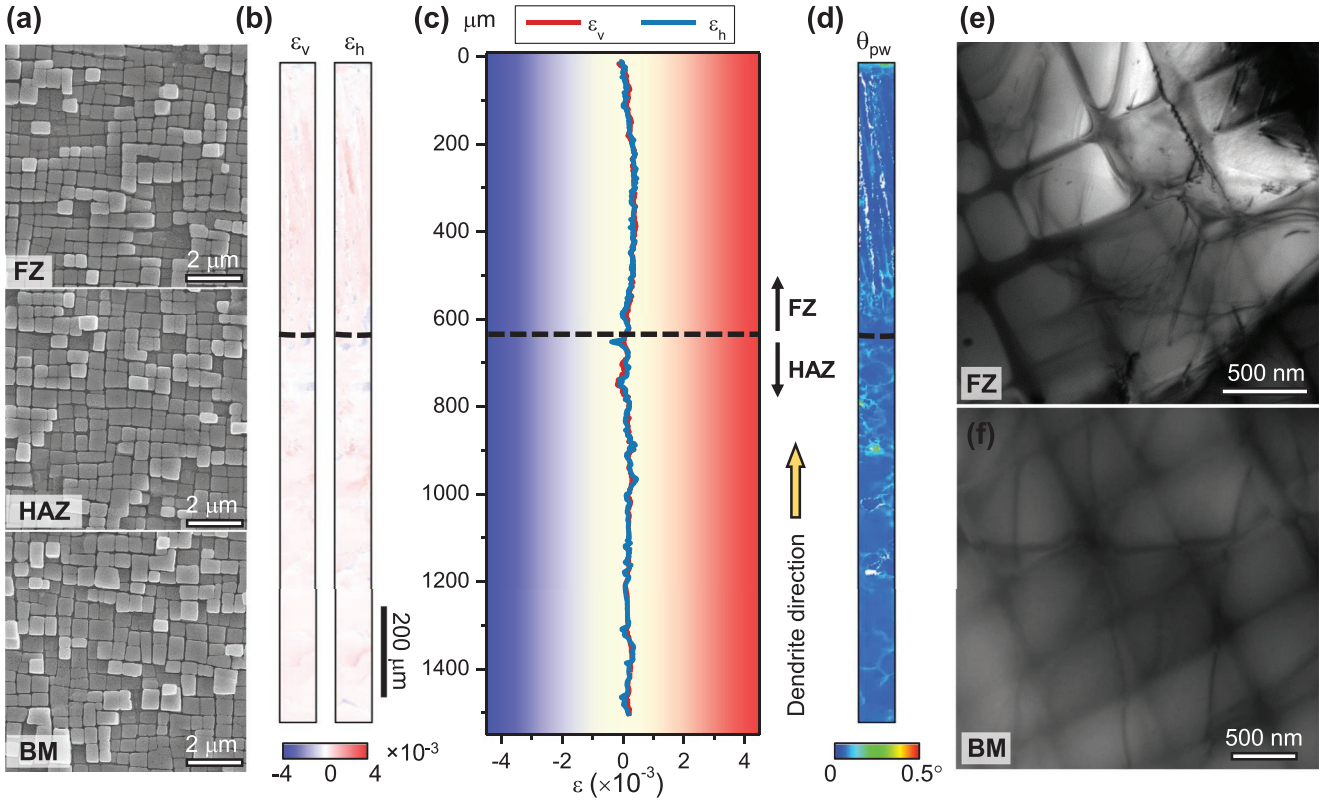

Figure 4. Uniform distributions of γ' morphology, elastic strain, and dislocations after full HT following our new protocol incorporating recovery annealing. a) Indistinguishable SEM images of γ' precipitates in the FZ, HAZ, and BM. b,c) μXRD demonstrates completely relieved strain, and d) the uniform and sharp diffraction peaks indicate low dislocation density (except at dendrite boundaries). The fusion line is marked with a dashed line in (b)–(d). e,f) TEM images indicate significant reduction in dislocation density in the HAZ (e), while the BM remains almost dislocation free (f).

uniform, exhibiting identical morphology and size. As seen in **Figure 4**a, they all have cubical shape with sharp vertices, straight edges, and uniform side length of about 500 nm. The γ' precipitates grow during the aging HT, becoming larger than those in the BM of the EBM sample. From the microindentation test results shown in Figure S7 in the Supporting Information, after HT with recovery the hardness is also uniform throughout, all the way from the FZ to the HAZ and to the BM, in stark contrast to the nonuniform hardness distribution in the EBM sample due to the pronounced spatial variation of the γ' precipitates size and morphology (Figure 3a) as well as of the dislocation density. μXRD results prove that the residual strain is fully released, evidenced by the uniform light color in the 2D maps, Figure 4b. There is only slight variation in the 1D strain profile of Figure 4c. The dislocation density in the HAZ and the FZ is also brought down significantly. The TEM image in Figure 4e shows a dislocation density of 2×10^{13} m^{-2}. Multiple TEM images are taken from the HAZ, two of which are displayed in Figure S8 in the Supporting Information. From these different regions the average dislocation density in the HAZ is found to be about 3×10^{13} m^{-2}, and in all TEM images it never exceeds 5×10^{13} m^{-2}. In other words, compared to the as-prepared EBM sample, the dislocation density decreases by more than 20 times in the HAZ. The BM, similar to the as-prepared sample, stays dislocation free (Figure 4f).

Before discussing the mechanism involved to accomplish dislocation removal, the microstructure after recovery annealing at 1100 °C for 6 h is studied in detail. As shown in **Figure 5**, rafted structure is observed almost everywhere in the FZ and the HAZ. Rafting is a common occurrence well known in superalloys subjected to external stresses and elevated temperatures.[30] It can also be induced by residual stresses in the specimens subjected to plastic prestrain and subsequent annealing.[31,32] In our case, the rafting is facilitated by the directional atomic diffusion driven by the residual stresses built-in during the EBM. The recovery annealing is carried out at a temperature close to the typical creep testing temperature for this superalloy.[33] Three typical rafted γ' microstructures (demonstrated in Figure 5a), which are recorded in the upper FZ, near the FZ/HAZ interface, and in the lower HAZ, respectively, are examined in detail. For AM3, a superalloy with negative lattice mismatch, the rafting direction is expected to be perpendicular to the tensile stress direction. In the upper FZ region, both horizontally and vertically rafted structures are observed, agreeing well with the observed spatial variation of the strain tensor and the sign (stress direction) displayed in Figure 3. Near the interface between the FZ and HAZ, vertically rafted structure forms. This is also consistent with the measured horizontal tensile strain in this region. As the strain direction reverses sign in the lower HAZ, the rafting direction changes as well. In confirmation, the strains in the recovery-annealed specimen are

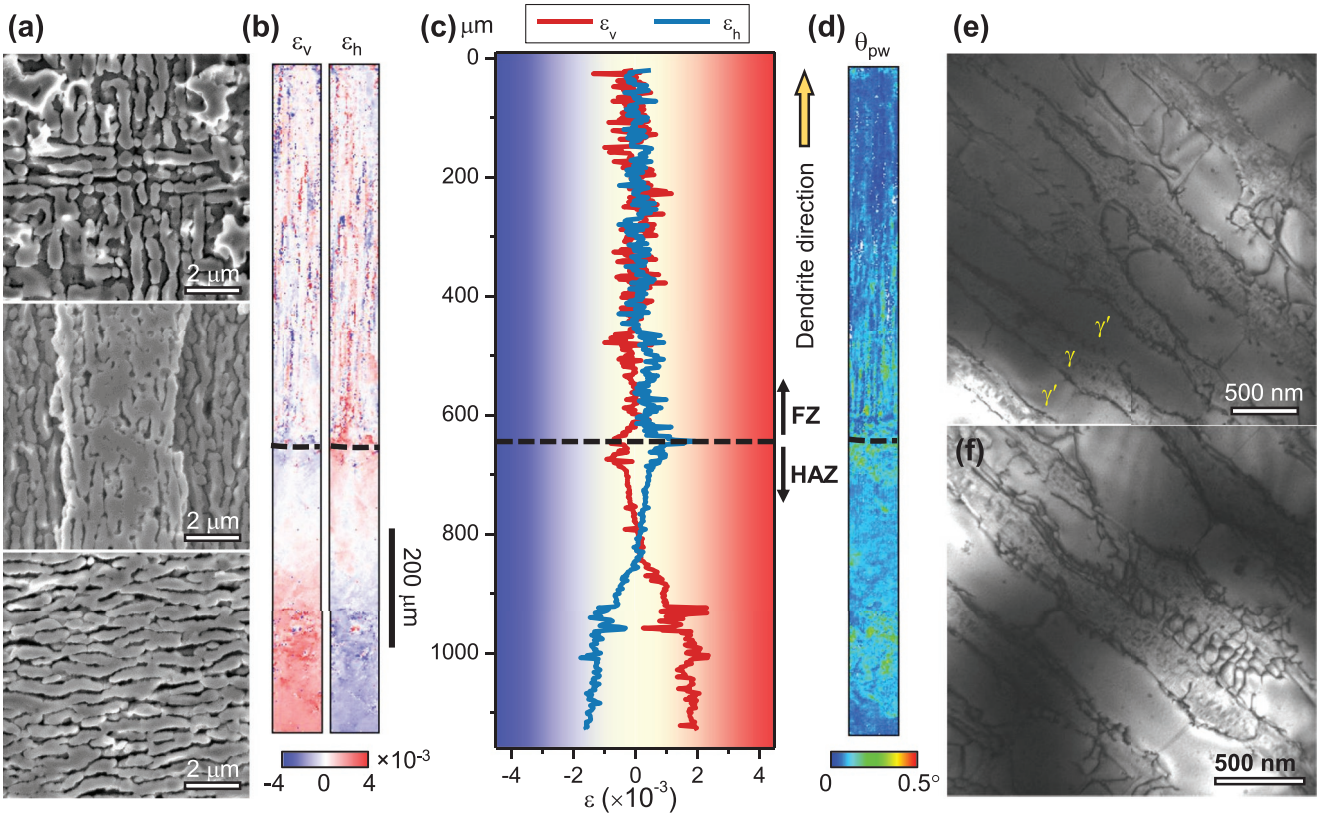

Figure 5. γ' morphology, elastic strain, and dislocations after 1100 °C recovery annealing. a) Rafted γ' observed in various directions. b–d) μXRD shows lowered strain in 2D (b) and 1D (c) profiles, as well as reduced diffraction peak width (d). The fusion line is marked by dashed line in (b)–(d). e,f) TEM observation illustrates dislocations rearranged at γ/γ' interfaces (e) and as networks (f). These are presumably low-energy dislocation configurations that can readily annihilate upon solution treatment, and the dislocation densities in these two images are almost one order of magnitude lower than that in the HAZ of the EBM sample.

significantly reduced, suggesting that the elastic strain energy stored in the EBM sample is effectively released along with rafting when the γ/γ' phase boundaries migrate (Figure 5b,c). The peak width map indicates that there are residual dislocations in the HAZ and the lower FZ (Figure 5d), thus TEM is employed for direct observation. As shown in Figure 5e,f, dislocations now line up at γ/γ' phase boundaries, and dislocation networks are also observed occasionally. In the literature, these two types of dislocation configurations were reported in superalloys after creep testing.[34,35] The dislocation density near these interfaces is measured to be 9×10^{13} and 2×10^{14} m^{-2}, respectively, but still up to one order of magnitude lower than that in the HAZ of the EBM sample. Taken together, the μXRD and TEM observations suggest that the combined rafting recovery is akin to that due to creep.[30,36,37] Note here again that previous annealing efforts were only able to achieve limited recovery, especially for regions that experienced rather high prestrains in plastic deformation.[38,39] Most of the previous attempts apparently have missed the appropriate temperature window, as they were unaware of the potential role that could be played by the rafting of γ' particles.

Regarding the role of rafting, it is in fact the migration of the γ/γ' phase boundaries that has ushered in a new mechanism to facilitate dislocation recovery. First, many dislocations sink into the interphase boundaries as they sweep by. Second, more spaces are opened for dislocation motion, as rafting widens some γ channels to accommodate dislocation movement and interactions that lead to annihilation. Third, the residual dislocations rearrange into lower-energy configurations at the γ/γ' interfaces (Figure 5) and these aggregated dislocation bundles re-configure more readily upon subsequent solution treatment at higher temperatures, as they no longer need to run across γ' precipitates to annihilate. This reduction of concentrated dislocations storing high energy leaves few spots as suitable RX nucleation sites, such that the ensuing solution treatment no longer sets off RX.

In previous reports, many attempts have been made to achieve stress relief and dislocation density reduction in superalloy single crystals to avoid RX. However, no completely successful example has been reported, because the recovery annealing temperature was either too low (below 1000 °C)[40] or too high (over the γ' solvus temperature).[26] Cyclic recovery annealing was also employed but proved to be inefficient to reduce the driving force for RX.[25] The recovery HT protocol reported in this study may be applicable to not only EBM, but also other 3D-printing scenarios. To demonstrate this, epitaxial AM3 layers were also manufactured using the direct laser-forming method on top of the cast BM with the same dimensions as those for the EBM case. The subsequent HTs are the same, incorporating the same recovery annealing. Homogeneous γ' precipitates are again obtained in all

the FZ, HAZ, and BM regions, without any sign of RX, as shown with EBSD examination results in Figure S9 in the Supporting Information.

Furthermore, although the recovery annealing costs 6 h, it is only a minor extension to the standard HT, which involves solution treatment at 1300 °C for 3 h followed by two steps of ageing at 1100 and 870 °C for 6 and 20 h, respectively. The inserted recovery step is thus only a simple addition, with little additional cost while effectively curtailing the undesirable RX.

Finally, we mention in passing a tweak to the recovery approach to lower the dislocation density and hence the RX driving force: the substrate can be heated in situ along with the 3D-printing (using electron beam, laser, or other heating resource) process. This in situ heating has shown its potential in one-step manufacturing of newly designed/tailored Ti alloy and maraging steel,[41,42] which does not require post-manufacturing HT and thus is expected to be cheaper and faster, although its application for repairing damaged superalloy single crystals has not been reported. Preheating may also lower the temperature for recovery annealing and shorten its duration, depending on the preheating conditions. However, substrate preheating at above 1000 °C is expected to be challenging for the requisite equipment (due to thermal drifts and corrosion), and also demands a stringent temperature control: a substrate temperature too high would diminish the temperature gradient, jeopardizing the epitaxial deposition. A temperature too low, on the other hand, would still incur too much deformation in local regions and hence too many stored dislocations in the HAZ. As such one would still need to add rafting-assisted recovery to suppress RX altogether. Our results in this paper demonstrate that the delicate control of preheating is not necessary. As a limiting case, simply using post-3D-printing recovery annealing alone, with no preheating at all, is already adequate to get rid of the normally expected RX. The post-EBM, presolutionizing recovery parameters (annealing temperature and time) can be adjusted depending on the stored dislocations that need to be recovered inside the printed/repaired alloy; a systematic documentation would however exceed the space limit of this Communication.

In summary, we have designed a new HT protocol to satisfy the requirement of "no RX together with uniform γ'," mandated for 3D-printing repair of Ni-based superalloy single crystals. Most essential in our strategy is the realization of subsolvus recovery prior to solution treatment, eliminating most of the stored energy that drives nucleation of new crystals during solution treatment. This is made possible by dislocation rearrangement and annihilation that are otherwise inactive in the absence of rafting γ'. Previous 3D-printing work to produce single-crystalline superalloys was not aware of, and did not take advantage of, this rafting vehicle for substantial recovery. Our finding thus opens an avenue to make additive manufacturing a widely applicable tool when dealing with the manufacture and repair of single-crystal superalloy part.

Experimental Section

EBM with no powder feeding was carried out using a DMAMS Zcomplex3 electron-beam 3D-printing system operated in 10^{-3} mbar vacuum. The substrate (BM) was cut into a cylinder 13 mm in diameter and 4 mm in height, from [001] cast single-crystal boules after solid solution HT. Electron beam of 15 mA was accelerated to 60 keV and focused onto the BM surface to form a melt pool. Line scanning was programmed at the velocity of 10–15 mm s^{-1} to ensure epitaxial dendrite growth in the melt pool. An FZ of about 1500 µm in width and 800 µm in depth was generated. The EBM sample was then recovery-annealed at 1100 °C for 6 h, solution-treated at 1300 °C for 0.5 h, and then aged at 1100 and 870 °C for 6 and 20 h, respectively. Note that although the solution treatment temperature was the same as the standard HT protocol, the duration needed was significantly shorter, because solute segregation in the EBM sample is much less than in its cast counterpart. Comparisons are made with an identical EBM sample heat treated without recovery, skipping the 1100 °C annealing step. This is the standard HT sample serving as the reference. The heating rate of all specimens was set at 15 °C min^{-1}. All samples were air cooled once the HT was finished.

Micro-hardness test was carried out using a Vickers hardness indenter under the force control mode, after EBM as well as after recovery annealing. On each specimen, a matrix of indentations covered the area from the BM to the FZ. Each indent was at least 4 µm deep to exclude the surface effect, and neighboring indents were 105 µm apart to make sure the hardness value was not influenced by the plastic deformation around adjacent indents.

Before and after recovery-HT, the microstructure was examined under secondary electron mode in a scanning electron microscope (SEM) after etching in 25% phosphoric acid water solution at the voltage of 5 V for 10 s. RX was monitored by mapping the crystal orientation of the sample surface using EBSD, after electrochemical polishing in 10% perchloric acid alcohol solution at the voltage of 20–30 V for about 60 s. µXRD sample was electro-polished the same way, and then scanned using micro-focused synchrotron polychromatic X-ray beam on Beamline 12.3.2 at the Advanced Light Source (ALS) of the Lawrence Berkeley National Laboratory.[43] The collected Laue diffraction data were processed using a custom-developed software based on the peak position comparison method to measure the strain tensor distribution accurately.[44] Diffraction peaks were identified based on a user-defined peak to background threshold. The position and width of each individual diffraction peak on the detector was determined by fitting intensity using a 2D Lorentzian function. By comparing the angles between experimentally measured diffraction peak positions with the theoretically calculated ones derived from unstrained and strained cubic lattice parameters, respectively, two 3×3 matrices were obtained, based on which a strain tensor was calculated using the equations derived previously.[45] The strain tensor obtained this way was the elastic lattice strain. The dislocation density maps were obtained semiquantitatively by plotting the Laue peak width distribution.[46] TEM specimens were prepared using the conventional twin-jet electropolishing.

Supporting Information

Supporting Information is available from the Wiley Online Library or from the author.

Acknowledgements

This work was supported by the National Natural Science Foundation of China (grant nos. 91860109, 51901026), and the National Key Research and Development Program of China (grant no. 2016YFB0700404). The authors also appreciate the support from the International Joint Laboratory for Micro/Nano Manufacturing and Measurement Technologies. E.M. is supported at JHU by NSF-DMR-1804320. The ALS was supported by the Director, Office of Science, Office of Basic Energy Sciences, Materials Science Division, of the U.S. Department of Energy under Contract No. DE-AC02-05CH11231 at LBNL. J.L. acknowledges support by NSF CMMI-1922206.

Conflict of Interest

The authors declare no conflict of interest.

Author Contributions

K.C., E.M., Z.W.S., and J.L. designed the project. R.H. conducted the EBM and direct laser forming experiments. R.H. and Y.L. developed the HT protocol for the EBM specimens. S.L. performed the HT on the direct laser forming sample. W.Z. carried out TEM and μXRD characterizations, and then analyzed and interpreted the μXRD data with R.H. under the supervision of K.C. and N.T. The paper was written by K.C., E.M., R.H., Z.W.S. and J.L. All authors contributed to discussions of the results.

Keywords

3D-printing, heat treatment, Ni-based superalloys, recovery protocols, recrystallization, single crystals

Received: October 31, 2019
Revised: December 18, 2019
Published online: February 20, 2020

[1] T. M. Pollock, *Nat. Mater.* **2016**, *15*, 809.
[2] B. L. Koff, *J. Propul. Power* **2004**, *20*, 577.
[3] S. S. Babu, N. Raghavan, J. Raplee, S. J. Foster, C. Frederick, M. Haines, R. Dinwiddie, M. K. Kirka, A. Plotkowski, Y. Lee, R. R. Dehoff, *Metall. Mater. Trans. A* **2018**, *49*, 3764.
[4] M. Gäumann, S. Henry, F. Cléton, J.-D. Wagnière, W. Kurz, *Mater. Sci. Eng., A* **1999**, *271*, 232.
[5] M. Gäumann, C. Bezençon, P. Canalis, W. Kurz, *Acta Mater.* **2001**, *49*, 1051.
[6] J. M. Vitek, *Acta Mater.* **2005**, *53*, 53.
[7] M. Ramsperger, C. Körner, in *Superalloys 2016* (Eds: M. Hardy, E. Huron, U. Glatzel, B. Griffin, B. Lewis, C. Rae, V. Seetharaman, S. Tin), Wiley, New York **2016**, pp. 341–349.
[8] Y. J. Liang, J. Li, A. Li, X. Cheng, S. Wang, H. M. Wang, *J. Alloys Compd.* **2017**, *697*, 174.
[9] Y.-J. Liang, X. Cheng, J. Li, H.-M. Wang, *Mater. Des.* **2017**, *130*, 197.
[10] C. Körner, M. Ramsperger, C. Meid, D. Bürger, P. Wollgramm, M. Bartsch, G. Eggeler, *Metall. Mater. Trans. A* **2018**, *49*, 3781.
[11] A. Basak, R. Acharya, S. Das, *Addit. Manuf.* **2018**, *22*, 665.
[12] T. Vilaro, C. Colin, J. D. Bartout, L. Nazé, M. Sennour, *Mater. Sci. Eng., A* **2012**, *534*, 446.
[13] M. Ramsperger, R. F. Singer, C. Körner, *Metall. Mater. Trans. A* **2016**, *47*, 1469.
[14] A. Basak, R. Acharya, S. Das, *Metall. Mater. Trans. A* **2016**, *47*, 3845.
[15] P. Nie, O. A. Ojo, Z. Li, *Acta Mater.* **2014**, *77*, 85.
[16] S. Gorsse, C. Hutchinson, M. Gouné, R. Banerjee, *Sci. Technol. Adv. Mater.* **2017**, *18*, 584.
[17] E. Chauvet, P. Kontis, E. A. Jägle, B. Gault, D. Raabe, C. Tassin, J.-J. Blandin, R. Dendievel, B. Vayre, S. Abed, G. Martin, *Acta Mater.* **2018**, *142*, 82.
[18] M. Ramsperger, I. Lopez-Galilea, R. F. Singer, W. Theisen, C. Körner, *Adv. Eng. Mater.* **2015**, *17*, 1486.
[19] S. Tadano, T. Hino, Y. Nakatani, *J. Mater. Process. Technol.* **2018**, *257*, 163.
[20] X. X. Yu, C. Y. Wang, *Acta Mater.* **2009**, *57*, 5914.
[21] C. Tian, G. Han, C. Cui, X. Sun, *Mater. Des.* **2014**, *64*, 316.
[22] S. L. Shang, C. L. Zacherl, H. Z. Fang, Y. Wang, Y. Du, Z. K. Liu, *J. Phys.: Condens. Matter* **2012**, *24*, 155402.
[23] F. Humphreys, M. Hatherly, *Recrystallization and Related Annealing Phenomena*, Elsevier, New York **2004**.
[24] Z. Li, Q. Xu, B. Liu, *Comput. Mater. Sci.* **2015**, *107*, 122.
[25] R. Bürgel, P. D. Portella, J. Preuhs, in *Superalloys 2000* (Eds: T. M. Pollock, R. D. Kissinger, R. R. Bowman, K. A. Green, M. McLean, S. Olson, J. J. Schirra), TMS, Warrendale, PA, USA **2000**, pp. 229–238.
[26] Z. L. Li, Q. Y. Xu, J. C. Xiong, J. R. Li, B. C. Liu, in *Materials Science Forum*, Vol. *850* (Eds: Y. Han, Y. Wu, G. Li, F. S. Pan, R. Fan, X. Liu), Trans Tech Publications Ltd., Stäfa-Zürich, Switzerland **2016**, pp. 47–55.
[27] D. C. Cox, B. Roebuck, C. M. F. Rae, R. C. Reed, *Mater. Sci. Technol.* **2003**, *19*, 440.
[28] D. M. Norfleet, D. M. Dimiduk, S. J. Polasik, M. D. Uchic, M. J. Mills, *Acta Mater.* **2008**, *56*, 2988.
[29] Y. Li, K. Chen, N. Tamura, *Mater. Des.* **2018**, *150*, 171.
[30] F. R. N. Nabarro, *Metall. Mater. Trans. A* **1996**, *27*, 513.
[31] M. Fährmann, E. Fährmann, O. Paris, P. Fratzl, T. M. Pollock, in *Superalloys 1996* (Eds: R. D. Kissinger, D. J. Deye, D. L. Anton, A. D. Cetel, M. V. Nathal, T. M. Pollock, D. A. Woodford), TMS, Warrendale, PA, USA **1996**, pp. 191–200.
[32] N. Ratel, G. Bruno, P. Bastie, T. Mori, *Acta Mater.* **2006**, *54*, 5087.
[33] S. Steuer, Z. Hervier, S. Thabart, C. Castaing, T. M. Pollock, J. Cormier, *Mater. Sci. Eng., A* **2014**, *601*, 145.
[34] J. X. Zhang, J. C. Wang, H. Harada, Y. Koizumi, *Acta Mater.* **2005**, *53*, 4623.
[35] L. Dirand, J. Cormier, A. Jacques, J. P. Chateau-Cornu, T. Schenk, O. Ferry, P. Bastie, *Mater. Charact.* **2013**, *77*, 32.
[36] M. Kamaraj, *Sadhana* **2003**, *28*, 115.
[37] N. Matan, D. C. Cox, C. M. F. Rae, R. C. Reed, *Acta Mater.* **1999**, *47*, 2031.
[38] S. D. Bond, J. W. Martin, *J. Mater. Sci.* **1984**, *19*, 3867.
[39] G. Xie, J. Zhang, L. H. Lou, *Prog. Nat. Sci.: Mater. Int.* **2011**, *21*, 491.
[40] C. Qiu, N. D'Souza, J. Kelleher, C. Panwisawas, *Mater. Des.* **2017**, *114*, 475.
[41] P. Kürnsteiner, M. B. Wilms, A. Weisheit, P. Barriobero-Vila, E. A. Jägle, D. Raabe, *Acta Mater.* **2017**, *129*, 52.
[42] P. Barriobero-Vila, J. Gussone, A. Stark, N. Schell, J. Haubrich, G. Requena, *Nat. Commun.* **2018**, *9*, 3426.
[43] M. Kunz, N. Tamura, K. Chen, A. A. MacDowell, R. S. Celestre, M. M. Church, S. Fakra, E. E. Domning, J. M. Glossinger, J. L. Kirschman, G. Y. Morrison, D. W. Plate, B. V. Smith, T. Warwick, V. V. Yashchuk, H. A. Padmore, E. Ustundag, *Rev. Sci. Instrum.* **2009**, *80*, 035108.
[44] N. Tamura, in *Strain and Dislocation Gradients from Diffraction. Spatially-Resolved Local Structure and Defects* (Eds: R. Barabash, G. Ice), World Scientific, London, UK **2014**, pp. 125–155.
[45] A. Pavese, *Phys. Chem. Miner.* **2005**, *32*, 269.
[46] J. Kou, K. Chen, N. Tamura, *Scr. Mater.* **2018**, *143*, 49.

ADVANCED MATERIALS

Supporting Information

for *Adv. Mater.*, DOI: 10.1002/adma.201907164

Rafting-Enabled Recovery Avoids Recrystallization in 3D-Printing-Repaired Single-Crystal Superalloys

Kai Chen, Runqiu Huang, Yao Li, Sicong Lin, Wenxin Zhu, Nobumichi Tamura, Ju Li,* Zhi-Wei Shan,* and Evan Ma**

Supporting information for

Rafting-enabled recovery avoids recrystallization in 3D-printing-repaired single-crystal superalloys

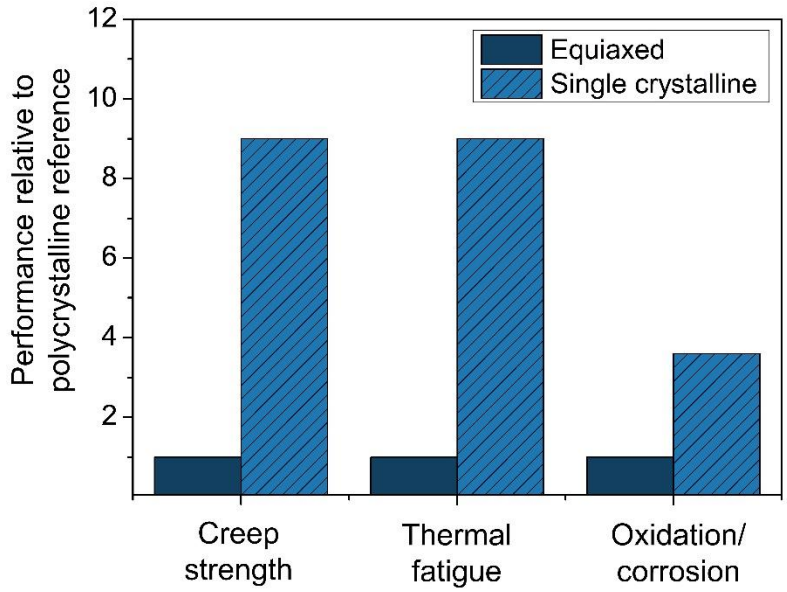

Figure S1 Comparison between polycrystalline and single crystalline Ni-based superalloys in terms of creep strength, thermal fatigue life, and oxidation/corrosion resistance [1].

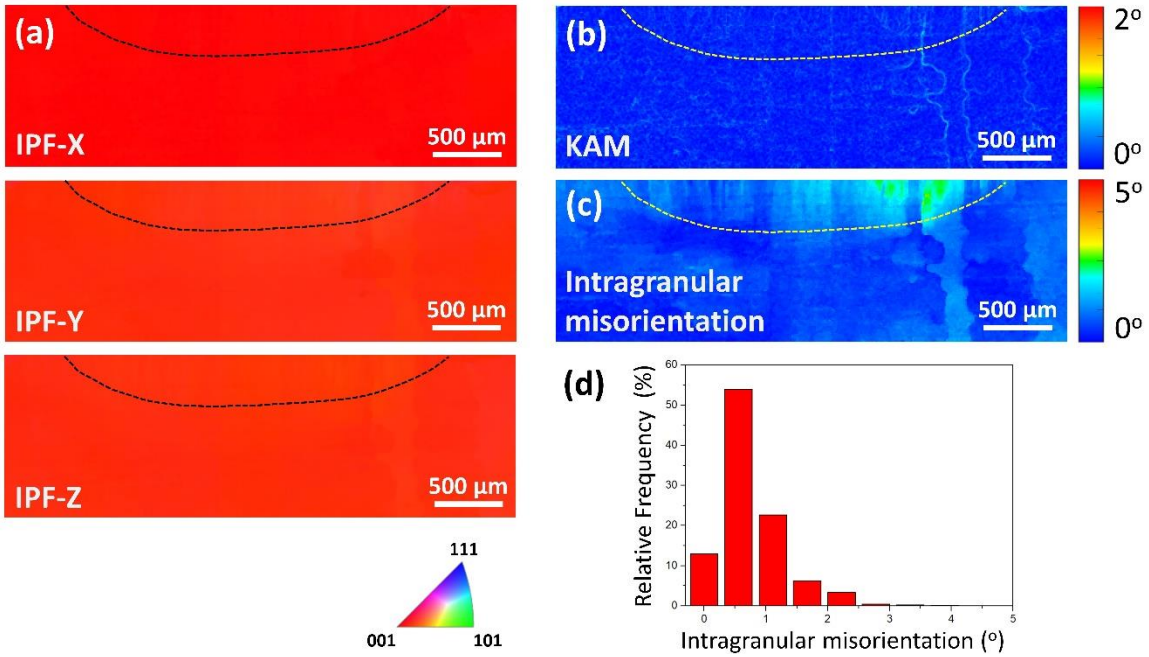

Figure S2 Microstructure study of the EBM sample using EBSD method. (a) Inverse pole figures (IPFs) in the horizontal (IPF-X), vertical (IPF-Y), and out-of-plane (IPF-Z) direction proves the single crystalline nature. The dotted curve indicates the HAZ/FZ interface. (b) The kernel average misorientation (KAM) map shows uniform orientation distribution in the dendrite cores while relatively higher misorientation at the interdendritic regions. KAM is defined as the average misorientation angle of a certain scanning position with its eight nearest neighbor positions [2]. (c) The intragranular misorientation map shows high misorientations in the FZ, and thus high defect density. Intragranular misorientation at each scan position is calculated as the misorientation angle between the measured crystal orientation and the average orientation of the grain. (d) The intragranular misorientation is studied statistically and displayed in histogram.

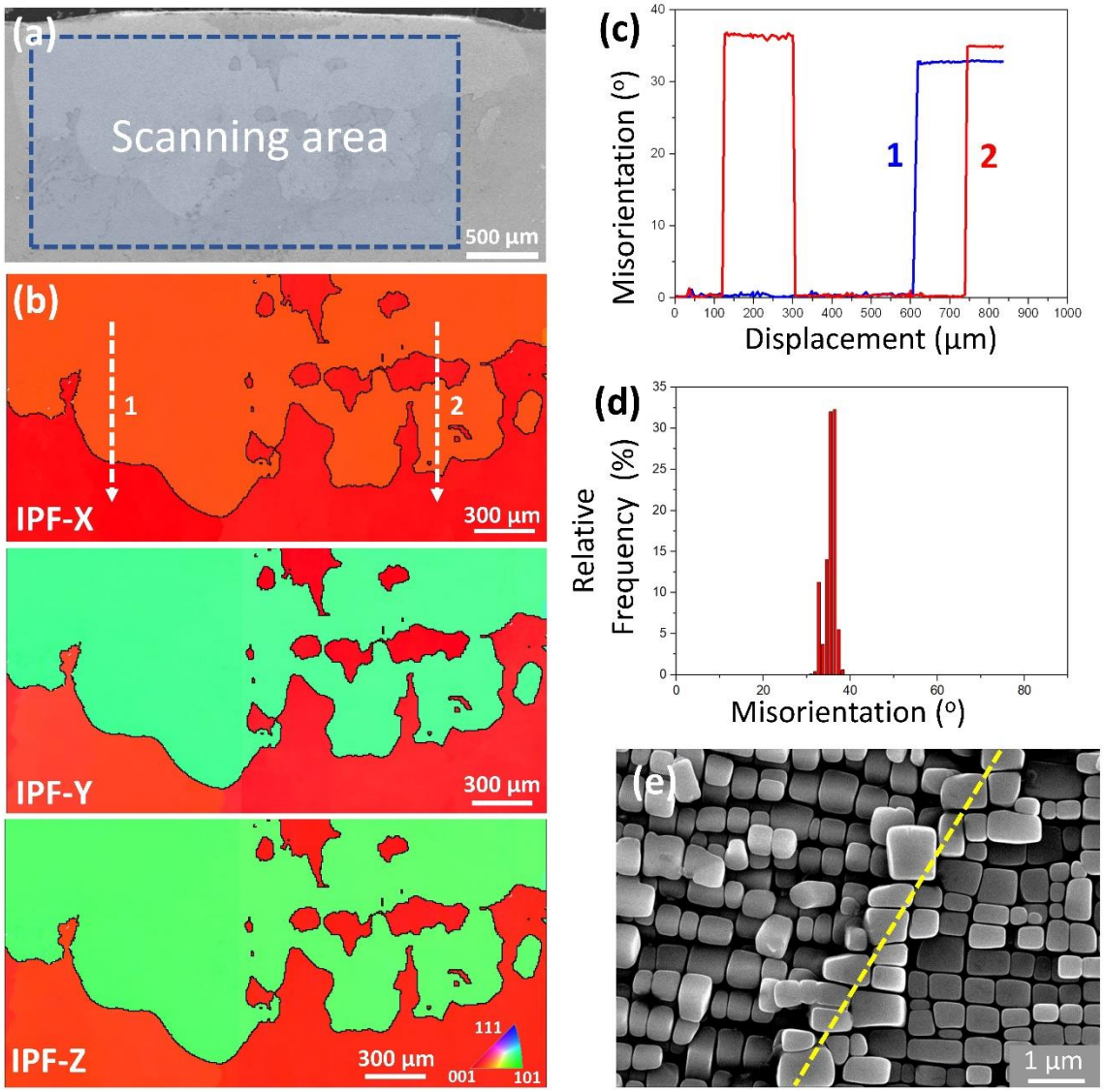

Figure S3 Misorientation study of a recrystallized sample after standard solution HT using EBSD technique. (a) High angle grain boundaries are visible in the low-magnification SEM image, with EBSD scanned region indicated. (b) High angle grain boundaries are clearly seen in the IPFs. (c) Misorientation distribution along two vertical lines indicated in the IPF-X map. (d) Misorientation statistical histogram evidences that the misorientations in the scanned region range from 30 ^{o} to 40^{o}. (e) Misorientation across the high angle grain boundary (indicated by the dotted yellow line) is seen from the orientation change of the cuboidal γ′ particles in the high-magnification SEM image.

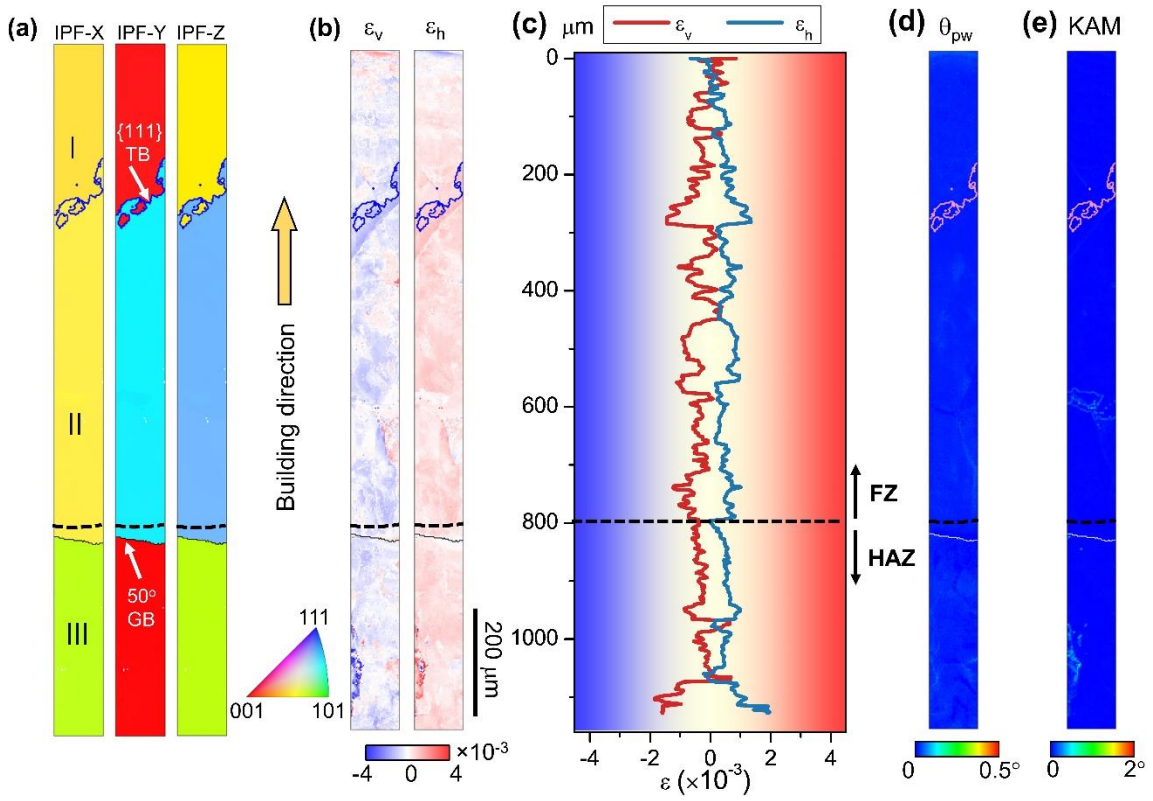

Figure S4 Microstructure study of a recrystallized sample after standard solution HT (the same processing parameter as the sample shown in Figure S3 but a different sample) using synchrotron radiation μXRD technique. (a) Three grains are identified and marked as I, II, and III, in the IPFs. The high angle grain boundaries are characterized as {111} twin and ordinary grain boundaries, respectively. The residual strain values are low and relatively uniform, as displayed in the (b) 2D and (c) 1D maps. (d) The average width of the Laue diffraction peaks and (e) the KAM are uniform and low, indicating low defect density in the sample after RX.

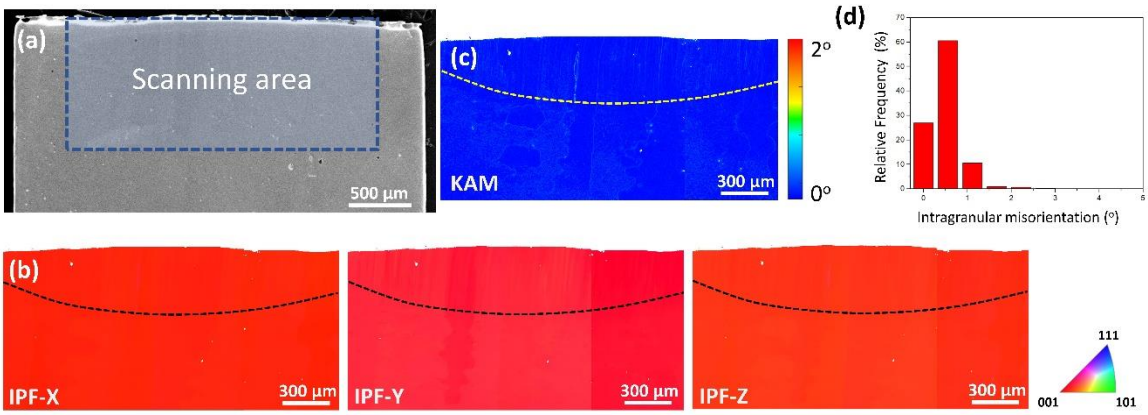

Figure S5 The orientation characterization of the sample after our new HT protocol. (a) The low magnification SEM image shows uniform contrast with no grain boundaries. The EBSD scanned area is indicated. (b) The IPFs shows no orientation variation in all three dimensions, which is further evidenced from (c) the KAM map. (d) Statistics proves that the misorientation in the heat treated sample becomes smaller than that in the EBM sample.

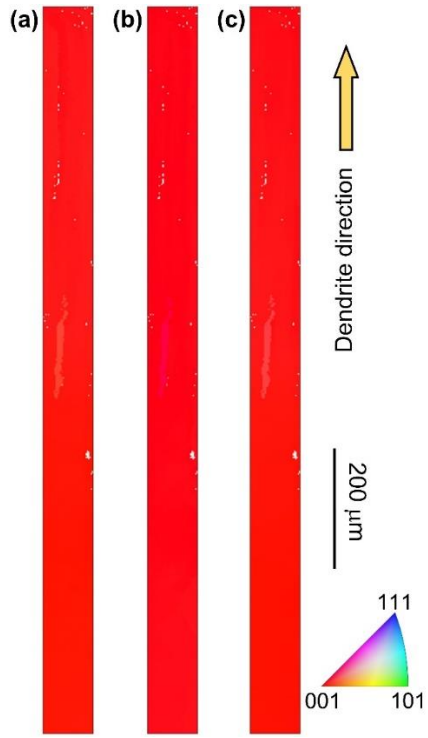

Figure S6 IPFs of the EBM sample in (a) horizontal, (b) vertical, and (c) out-of-plane directions studied using μXRD method.

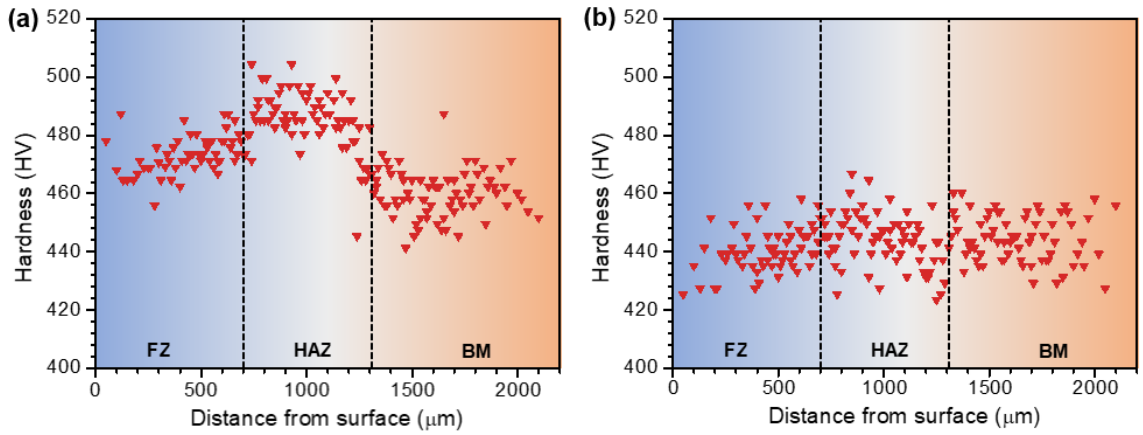

Figure S7 Vickers hardness distribution measured in samples after (a) EBM and (b) full heat treatment incorporating recovery annealing.

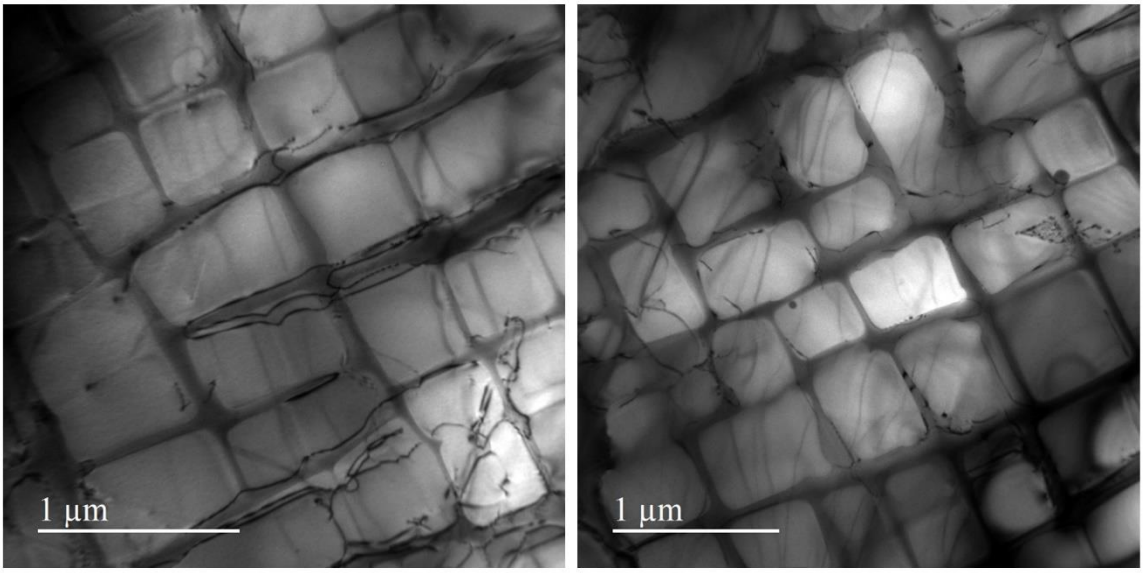

Figure S8 TEM observation of the dislocations in the HAZ after full HT following our new protocol incorporating recovery annealing. The dislocation densities in these images are measured to be approximately 5×10^{13} m^{-2} and 2×10^{13} m^{-2}, respectively.

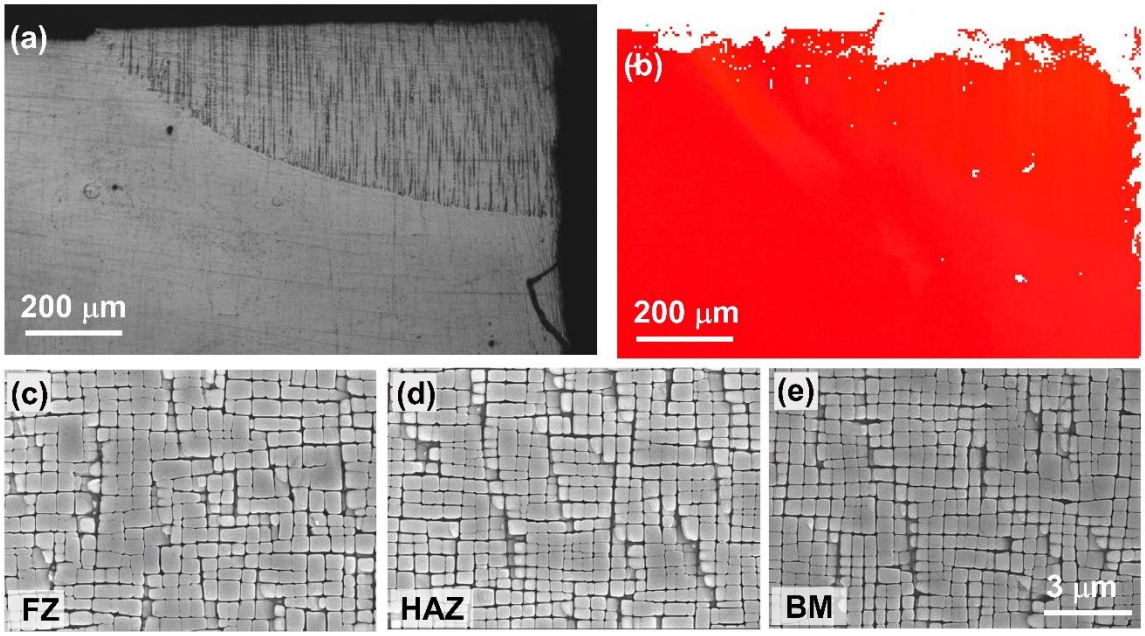

Figure S9 Microstructure characterization of the epitaxial AM3 Ni-based superalloy manufactured using the direct laser forming method on top of cast BM. The melt pool was generated by scanning the BM surface approximately along the [010] direction using a Nd: YAG laser at 5 mm/s. The beam size and power of the laser were 2 mm in diameter and 550 W, respectively. The laser power and scanning speed were optimized to ensure epitaxial growth without crack formation. (a) Optical micrograph of the as-fabricated sample that was cut along the laser scanning direction from approximately the middle of the melt pool. (b) Crystal orientation map obtained using EBSD of roughly the same region as shown in (a) after full HT following our new protocol incorporating recovery annealing, proving that RX has also been successfully prevented. (c-e) SEM images showing uniform γ' precipitates in the FZ, HAZ, and BM, respectively, after full HT and etching in 25% phosphoric acid water solution at the voltage of 5 V for 10 s.

Reference:

[1] B. L. Koff, *J. Propuls. Power* **2004**, *20*, 577.
[2] C. Moussa, M. Bernacki, R. Besnard, N. Bozzolo, *IOP Conf. Ser.: Mater. Sci. Eng.* **2015**, 89, 012038.